Simultaneous Catalytic Construction of Closed-Pore-Rich Hard Carbon Anode and Generation of $Na_{0.67}Ni_{0.2}Fe_{0.2}Mn_{0.6}O_2$ Cathode for Sodium-Ion Batteries

Tianzhuo Wen, Shimin Yan, Liangyu Li, Yan Ding, Jing Li, and Zhongxue Chen*

Sodium-ion battery (SIB) has been regarded as a promising electrochemical device for stationary energy storage, whereas its widespread application is still hindered by relatively lower energy density and unredeemed cost-effectiveness. High-capacity anode materials are one of the bottlenecks limiting the improvement of energy density of SIBs, while tuning the closed porous structure is the most efficient approach to boost the plateau capacity. Unfortunately, simple and practical closed-pore-forming strategies remain scarce. Herein, a transition metal oxide catalytic strategy to prepare closed-pore-rich hard carbon anode for the first time while simultaneously transforming the catalyst into layered oxide cathode is reported. The abundant closed-pore structure provides an augmented array of sites for sodium ion storage, thereby contributing to a heightened plateau capacity and Coulombic efficiency. Hence, the obtained anode delivers a reversible capacity of 301.6 mAh g^{-1} with a high initial coulombic efficiency of 92.3%. Note that a capacity retention of 98.4% is achieved after 300 cycles. In particular, a full cell constructed by the above closed-pore-rich hard carbon anode and layered oxide cathode demonstrates favorable energy density and cycling stability. This work is believed to provide a green and sustainable route for achieving high-performance SIB electrode materials.

1. Introduction

The growing development of renewable energy has created increasing demand for low-cost, large-scale energy storage systems.[1–4] Although lithium-ion batteries have been widely adopted in electric vehicles and portable electronics due to their high energy density and environmental friendliness,[5] their application in large-scale energy storage systems is hindered by the low crustal abundance and uneven geographical distribution of lithium resources.[6,7] In recent years, sodium-ion batteries (SIBs) have attracted significant attention owing to their cost-effectiveness, resource abundance, and similar working mechanism to lithium-ion batteries.[8–11] Anode material is one of the most important component to determine the performance of SIBs. To date, a variety of anode materials based on different Na$^+$ storage mechanisms have been proposed for SIBs, including intercalation, conversion, and alloying types.[12] As a representative

intercalation anodes, hard carbon (HC) owns the merits of low working voltage, high conductivity, environmental friendliness, and abundant resources,[13] therefore taking the lead in entering the commercial manufacturing process. However, HC anode still suffers from low initial Coulombic efficiency (ICE) and unsatisfactory low-voltage plateau capacity, which substantially restrains the energy density and energy conversion efficiency of SIBs.

The sodium storage behavior of the HC anode is directly determined by its microstructure.[14–16] As is well-known that HC has a large-spaced disordered layer structure in which huge amounts of randomly oriented, twisted, and defect-rich graphite-like amorphous nanodomains are complexly arranged.[17–19] This complicated structure on the one hand puts forward rigorous requirements on the controllability and consistency of production, on the other hand, leads to elusive reaction mechanism. Despite sophisticated structure-performance correlation, the sloping and plateau capacity of the HC anode are commonly recognized to be related to the turbostratic structure and internal closed pore, respectively. Considering that the plateau capacity in low-voltage regions is the main contributor to improving the energy density of SIBs, closed-pore structure engineering is regarded as an effective strategy to enhance the plateau capacity of the HC anode.[20,21]

Currently, the general preparation methods for constructing closed pores in HC include preoxidation[18] and introducing pore-forming agents.[22] Preoxidation treatment can introduce oxygen-containing functional groups into the precursor and prevent the growth of graphite layer rearrangement during the carbonization process, thus promoting the formation of closed pores.[23–25] However, the number of closed pores generated by preoxidation treatment is always insufficient, hence the effect of increasing

T. Wen, S. Yan, L. Li, Z. Chen
School of Power and Mechanical Engineering
Wuhan University
Wuhan 430072, China
E-mail: zxchen_pmc@whu.edu.cn

Y. Ding
College of Chemistry and Molecular Sciences
Wuhan University
Wuhan 430072, China

J. Li
School of Chemistry and Chemical Engineering
Ningxia University
Yinchuan 750021, China

Batteries & Supercaps

Research Article
doi.org/10.1002/batt.202500715

Chemistry Europe
European Chemical
Societies Publishing

plateau capacity is limited. Compared with preoxidation, the strategy of introducing pore-forming agents favors to producing abundant closed pores.[26,27] Hard templates, activation reagents, and organics have been successively employed as the pore-forming agents, which substantially improve the plateau capacity of HC anode.[28] Unfortunately, these approaches usually require cumbersome pretreatment or post-treatment, which will inevitably increase production costs and uncontrollability. Besides, the pore-forming process often involves the usage of harmful reagents and releases considerable waste, thereby posing a risk of environmental pollution. In this context, there is an urgent need to develop a green and sustainable method for preparing HC with a closed-pore structure.

In this work, we report for the first time the synthesis of closed-pore-rich HC by catalyzing the pyrolysis of walnut shells with the mixture of transition metal oxides (NiO, Fe_2O_3, and Mn_2O_3). The catalytically carbonized HC (CC-HC) anode can provide a reversible capacity of 301.6 mAh g^{-1} with a high ICE of 92.4%, and retain 98.4% of its initial capacity after 300 cycles. Molecular dynamics (MD) calculations reveal that the catalytic effect of transition metal oxides promotes the formation of abundant closed-pore structures, thereby contributing to the improved Coulombic efficiency and cycling stability. More significantly, unlike the discarded pore-forming agents in previous works, our approach in situ transforms the catalyst into layered oxide cathode $Na_{0.67}Ni_{0.2}Fe_{0.2}Mn_{0.6}O_2$ (NNFM), which delivers a reversible capacity of 130 mAh g^{-1}. Furthermore, the CC-HC|| NNFM full cell constructed by the above anode and cathode achieves an energy density of 206.7 Wh kg^{-1}.

2. Results and Discussion

2.1. Synthesis and Structural Characterization of CC-HC

Figure 1a schematically illustrates the two-step synthesis of a closed-pore-rich HC material. The walnut shells, as agricultural wastes, are used as raw material for activated carbon production, while a mixture of transition metal oxides (NiO, Fe_2O_3, and Mn_2O_3, with a molar ratio of 2:1:3) is employed as the catalyst. At the first step, the mixture of walnut shells and metal oxides is treated under an argon atmosphere at 600 °C. The resulting power is then washed by HCl to separate carbon from the transition metal oxides. During the second step, the obtained carbon is sintered at 1300 °C to generate the final product CC-HC. At the same time, the transition metal oxides catalyst is dissolved in HCl and mixed with $NaNO_3$. The mixture is then dried, followed by a calcination at 950 °C in a dry air atmosphere for 10 h to obtain
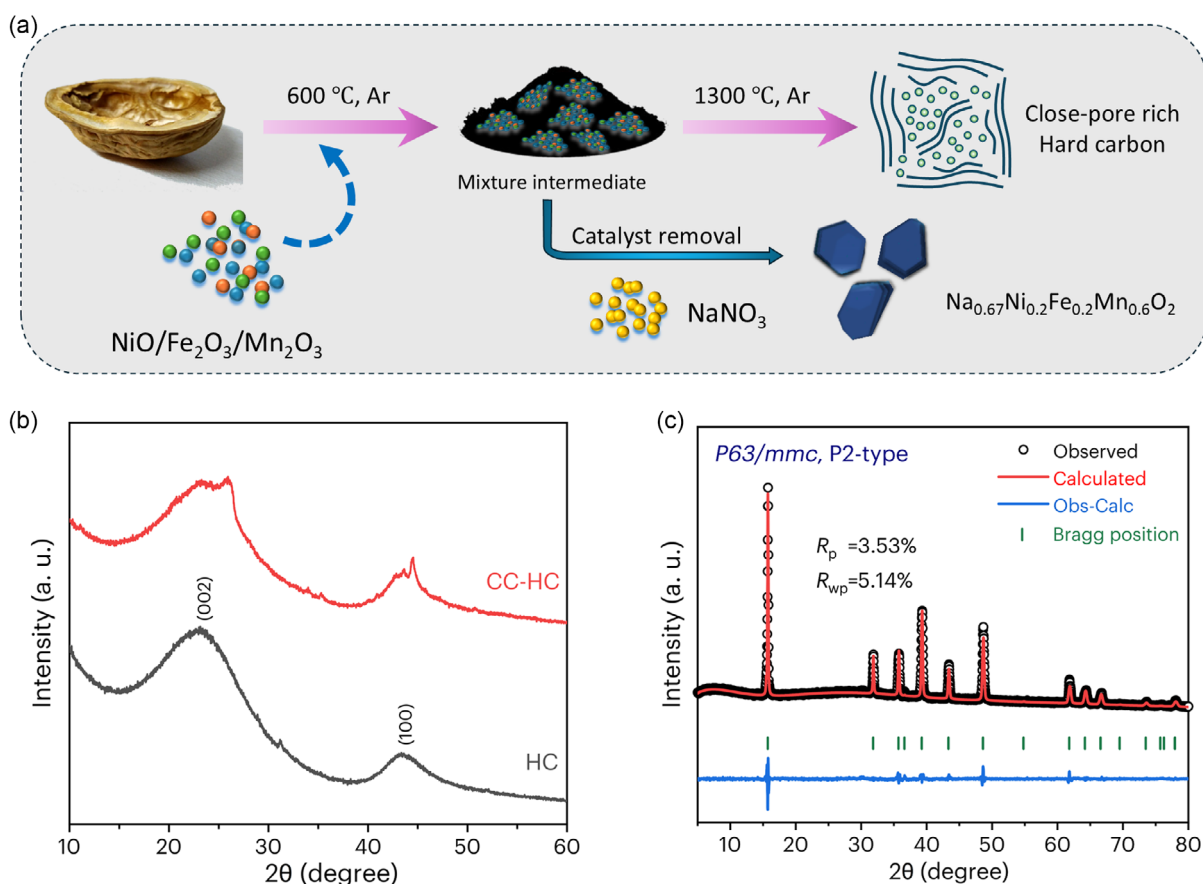

Figure 1. a) Schematic diagram for the simultaneous synthesis of a closed-pore-rich CC-HC and NNFM. b) The XRD patterns of HC and CC-HC. c) Rietveld refinement of XRD pattern of NNFM.

Batteries & Supercaps

Research Article
doi.org/10.1002/batt.202500715

Chemistry Europe
European Chemical
Societies Publishing

$Na_{0.67}Ni_{0.2}Fe_{0.2}Mn_{0.6}O_2$ (NNFM). This strategy realizes the simultaneous synthesis of CC-HC anode and NNFM cathode, and almost all raw materials are converted into final products, which is in line with the requirements of green and sustainable industrial production. In addition, a control sample (named as HC) is also prepared by the same procedure in the absence of transition metal oxide catalysts.

We first employ X-ray diffraction (XRD) to examine the crystal structures of the obtained anode and cathode. As displayed in Figure 1b, two broad peaks at ≈23° and ≈42° are observed for both HC and CC-HC, corresponding to the characteristic (002) and (100) crystal planes in the HC structure, respectively. Note that the XRD pattern of the CC-HC sample shows two sharp peaks at ≈26° and ≈44°, which are associated with an increased graphitization degree. The average d_{002} spacing of HC is calculated to be 0.385 nm according to the Bragg equation. The catalytic effect of transition metal oxides induces a more ordered microstructure, while the d_{002} interlayer spacing of CC-HC decreases to 0.373 nm due to the increased graphitization degree. Some earlier studies have found that HC with interlayer spacing distances of 0.37–0.40 nm has better sodium storage properties,[29] indicating that both HC and CC-HC will potentially offer a favorable sodium storage performance. The La and Lc values of the HC and CC-HC, calculated based on the Scherrer formula, increase from 2.508 and 1.150 nm to 2.587 and 1.280 nm, respectively, indicative of the formation of a large number of graphitized nanodomains. Figure 1c shows the XRD pattern with Rietveld refinement of NNFM. It can be seen that the NNFM has a typical P2-type layered structure with P63/mmc space group, and no impurity is detected, suggesting the transition metals in the catalyst are completely transformed into the final cathode. The small R factor

values ($R_p = 3.53\%$, $R_{wp} = 5.14\%$) confirm the satisfactory fitting results. The Rietveld refinement of the XRD pattern of NNFM yielded lattice parameters a and c of 2.896347 and 11.214412 Å, respectively. More detailed structure data on NNFM are listed in (Table S1, Supporting Information).

The morphological difference between HC and CC-HC is studied by scanning electron microscopy (SEM). As shown in Figure S1, Supporting Information, both HC and CC-HC samples show a smooth surface with diameters ranging from 4 to 6 μm. **Figure 2**a–c shows the high-resolution transmission electron microscopy (HRTEM) images of the two samples. A disordered structure that consists of randomly oriented and loosely stacked graphitic nanosheets (also called disordered turbostratic nanodomains) embedded in disordered amorphous regions is observed for the HC sample (Figure 2a), which is the structural characteristics of HC. The average interlayer spacing of HC measured based on fast Fourier transform (FFT) patterns is 0.385 nm. By contrast, CC-HC shows a narrower interlayer spacing of 0.372 nm (Figure 2b). It is noteworthy that more and curved carbon layers lead to the formation of numerous closed pores, which significantly enhances the sodium ion storage capacity. In addition, it is interesting that some ordered graphite lattice fringes are found in CC-HC (Figure 2c), which is in harmony with the characteristic peaks of graphite observed in XRD. The presence of closed pores and graphite lattice fringes both contributes to the electrochemical behavior of sodium ions.[30] The SEM image in Figure S2, Supporting Information, shows the lamellar morphology of NNFM with an average particle size of ≈2 μm. The energy-dispersive X-ray spectroscopy (EDX) mapping indicates that Na, Ni, Fe, Mn, and O elements are homogeneously distributed within the particles.
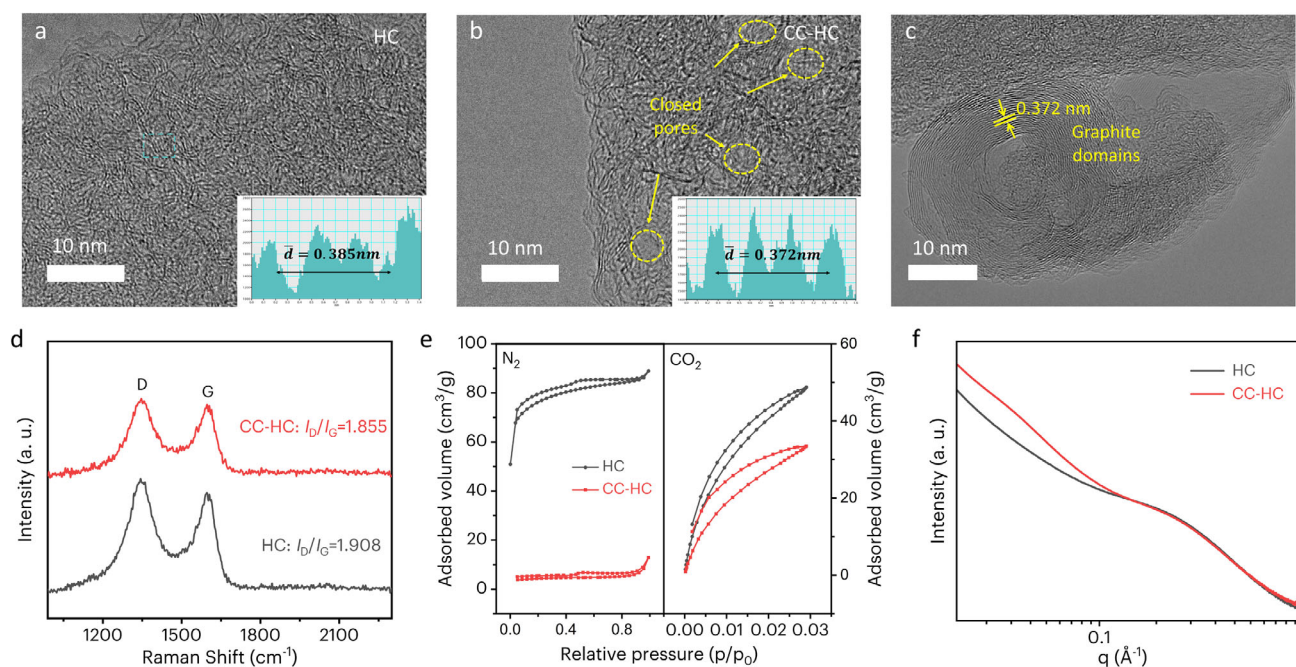

Figure 2. The high-resolution TEM images of a) HC and b,c) CC-HC. d) The Raman spectra, e) N_2 and CO_2 adsorption–desorption isotherms, and f) SAXS curves of HC and CC-HC.

The microstructure of HC and CC-HC is further characterized by Raman spectroscopy and X-ray photoelectron spectroscopy (XPS). The Raman spectra shown in Figure 2d consist of two characteristic bands at $\approx$1340 (D band) and $\approx$1590 cm^{-1} (G band), corresponding to the amorphous and graphitic structures of carbon materials, respectively.[31] The ratios of I_D/I_G are calculated to be 1.908 and 1.855 for HC and CC-HC, respectively (Figure S3, Supporting Information). The decreased I_D/I_G ratio signifies a higher degree of graphitization in the CC-HC sample, which is consistent with the above characterizations. XPS is then performed to quantitatively analyze the composition of functional groups in HC and CC-HC. As displayed in Figure S4, Supporting Information, the C 1s XPS spectra of the samples can be deconvoluted into C—C, C—O, and C=O located at 284.8, 285.5, and 286.8 eV, respectively. The fitted proportions of C—O are 76.4% for HC and 76.8% for CC-HC, respectively, while the fitted proportion of C=O increases from 10.3% for HC to 14.0% for CC-HC. Considering that C=O functional groups have been identified as effective active sites for sodium storage, the CC-HC is expected to manifest higher reversible capacity than HC.

The pore structure of HC and CC-HC is characterized by N_2 (77 K) and CO_2 (273K) adsorption–desorption tests. As shown in Figure 2e. The N_2 adsorption–desorption isotherms of both samples appear as a characteristic type-I shape, indicating that their pore structures are dominated by micropores. Note that the isotherm of CC-HC at low relative pressure becomes much weaker, and the Brunauer–Emmett–Teller (BET) specific surface area decreases significantly from 238 m^2 g^{-1} for HC to 13.38 m^2 g^{-1} for CC-HC. The ultramicropores of both samples are analyzed by using the CO_2 adsorption–desorption isotherm due to the faster diffusion rate of CO_2 at 273 K compared with that of N_2 at 77 K. The overall pore size distribution is calculated by using the nonlocal density functional theory equilibrium model (NLDFT) from the CO_2 ($<$1 nm) and N_2 ($>$1 nm) adsorption isotherms. As shown in Figure S5, Supporting Information, both samples have a microporous structure with pore sizes ranging from 0.4 to 1.0 nm, and the open pore volume shows a huge drop from 0.0892 cm^3 g^{-1} for HC to 0.0613 cm^3 g^{-1} for CC-HC. It is well-known that the adsorption/desorption of N_2 and CO_2 can only provide insight into the open porosity, but is not sensitive to the closed porosity of HC materials. To elucidate the characteristics of the closed pores, we conduct small-angle X-ray scattering (SAXS) to obtain the average pore size by fitting the test results. Figure 2f shows that there is a significant change in the shoulder peak at $\approx$0.1–0.5 Å^{-1} after the catalytic treatment with metal oxides, which originates from the micropores in the carbon block.[32] The size distribution of the closed pores is shown in Figure S6, Supporting Information, and the average diameters for HC and CC-HC are 1.11 and 1.07 nm, respectively. Furthermore, we determined the true density using the He displacement method, a standard technique for assessing pore volume. The true densities for HC and CC-HC are 2.2289 and 2.0895 g cm^3, respectively. Subsequently, the closed-pore volumes can be calculated using Equation (1) . The value of 2.26 is from the true density of ideal layered graphite without any pore structure.[33] The calculated closed-pore volume

significantly increases from 0.0062 cm^3 g^{-1} for HC to 0.0361 cm^3 g^{-1} for CC-HC. These results clearly demonstrate that the catalytic effect of metal oxides can effectively increase the closed-pore volume.

$$V_{closedpore} = \frac{1}{\rho_{true}} - \frac{1}{2.26} \qquad (1)$$

To illuminate the morphological difference of HC induced by the catalytic effects of metal oxides, conduct Quantum chemical calculation is further performed. When figuring out the binding energy between various transition metal oxides and carbon, graphene sheets are used to simulate carbon materials, and clusters represent transition metal oxides. Based on the lowest-energy structure, the relative binding energies of NiO, Fe_2O_3, and Mn_2O_3 with carbon are calculated to be -0.27, -0.40, and -0.37 eV, respectively (Figure S7, Supporting Information), confirming all three kinds of metal oxides' tendency to bond with carbon during catalytic carbonization. When the transition metal oxides are removed with strong acid, the graphene sheet will also form a defect structure under the erosion of acid (**Figure 3**a).

Next, we use the ab initio molecular dynamics (AIMD) to dissect the formation process of closed pores. Typical vacancy defects are utilized to denote defective graphene, with an initial interlayer distance set to $\approx$3.5 Å and a total of 186 carbon atoms. Additionally, three isolated carbon atoms are situated between the two layers of graphene. The initial model structure is illustrated in Figure 3b. As the temperature increases, the position of the carbon atoms in the graphene layer changes significantly due to the influence of the intermediate free carbon atoms. Some carbon atoms exhibit a "detachment" behavior from the graphene layer and approach another graphene layer to form a closed-pore structure (Figure 3c). The top view of the structural changes during the heating process is shown in Figure S8, Supporting Information. Figure 3d shows the distance from the carbon atoms in one graphene layer to another graphene layer, revealing that the distance of some carbon atoms is significantly smaller than that in the initial configuration. Interestingly, as illustrated in Figure S9, S10, Supporting Information, during the heating process, free carbon atoms fill the defect area of the graphene layer, resulting in partial graphitization of the carbon material. In conclusion, the catalytic effect of metal oxides induces defects in the material. After heat treatment, the defective carbon layer exhibits a distinct closed-pore structure and partial graphitization, which aligns with the previous characterizations.

2.2. Sodium Storage Behaviors in Half Cells

Electrochemical Na-storage properties of the obtained carbon materials are evaluated in half-cells. The cyclic voltammetry (CV) measurements are performed at a scan rate of 0.1 mV s^{-1} for HC and CC-HC electrodes. As shown in **Figure 4**a,b, both electrodes show a broad reduction peak in the potential region of 1.0–0.2 V (vs. Na$^+$/Na) and a sharp reduction peak in the potential region of 0.10–0.001 V (vs. Na$^+$/Na). According to previous researches, these two peaks are associated with the adsorption

Batteries & Supercaps

Research Article
doi.org/10.1002/batt.202500715

Chemistry Europe
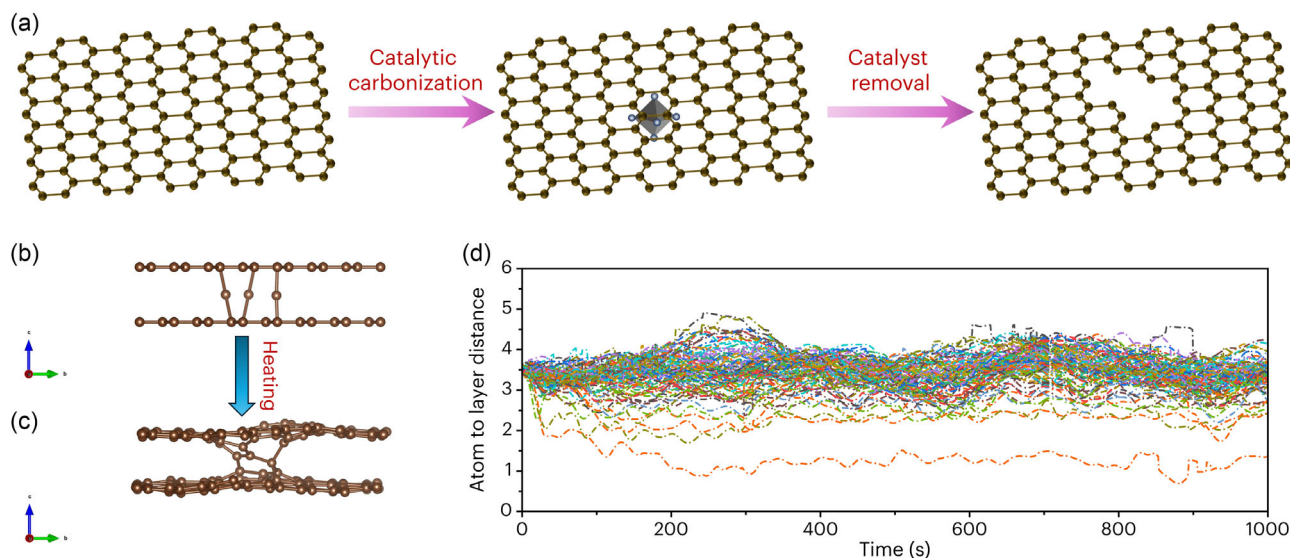European Chemical
Societies Publishing

Figure 3. a) Simulations showing the catalytic effect of transition metal oxides on the generation of defective graphene. Side view of b) pristine and c) heated defective graphene structure while forming closed-pore. d) The distance from carbon atoms to another graphene layer during the heating process.
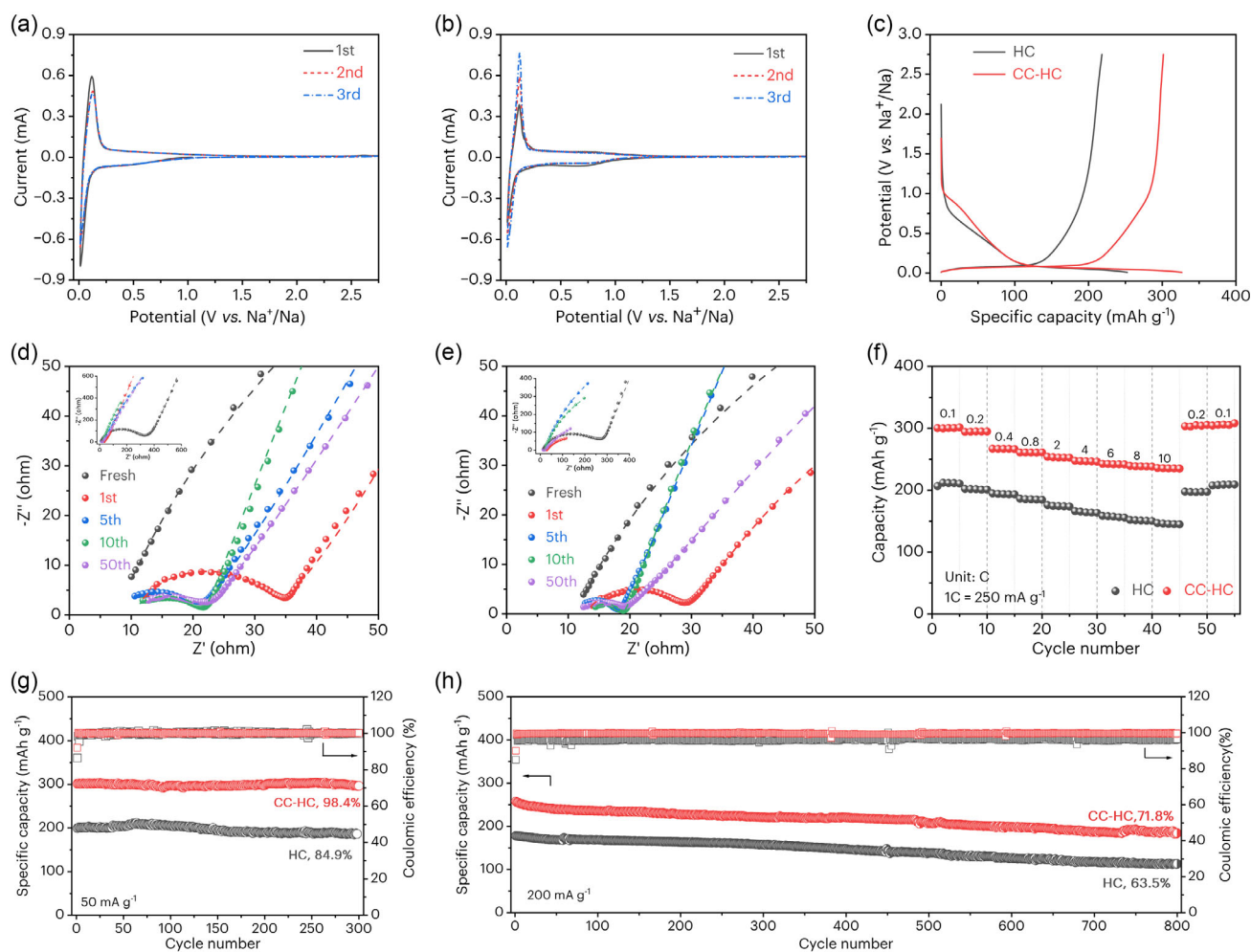

Figure 4. The electrochemical performance of HC and CC-HC. a,b) CV curves at 0.1 mV s^{-1}; c) the initial discharge–charge curves at a current density of 25 mA g^{-1}; d,e) the EIS spectra; f) the rate performance at different current densities from 0.1 to 10 C (1C = 250 mA g^{-1}); and g,h) cycling performances at current densities of (g) 50 mA g^{-1} and (h) 200 mA g^{-1}.

Batteries & Supercaps

Research Article
doi.org/10.1002/batt.202500715

Chemistry Europe
European Chemical
Societies Publishing

and intercalation/pore filling reactions of Na^+ in the HC. It should be noted that in the first cycle of Figure 4b, the irreversible reduction peak around 0.7 V is attributed to the irreversible decomposition of the electrolyte and the formation of the solid electrolyte interface (SEI) film.[34] In the following scans, the CV curves almost overlap, suggesting the stable Na storage performance of both anode materials. Figure 4c shows the initial charge and discharge profiles of HC and CC-HC electrodes at a current density of 25 mA g^{-1}. Two voltage platforms including a slope located in the voltage region of higher than 0.1 V and a rather flat plateau between 0.1 and 0.01 V are observed, which are consistent with the CV measurements. The reversible capacity and ICEs increase significantly from 218.1 mAh g^{-1} and 86.4% for HC to 301.6 mAh g^{-1} and 92.3% for CC-HC, respectively. Obviously, the enhanced electrochemical performance of CC-HC should be attributed to the abundant closed pores induced by the catalytic effect of transition metal oxides, which provide an augmented array of sites for sodium ion storage, thereby contributing to a heightened plateau capacity and Coulombic efficiency.[35]

The reaction kinetics of HC and CC-HC are subsequently evaluated using electrochemical impedance spectroscopy (EIS). As shown in Figure 4d,e, the Nyquist plots of both electrodes consist of a high-frequency semicircle and a low-frequency steeper line corresponding to the charge transfer resistance (R_{ct}) and Warburg impedance (Z_ω), respectively. The EIS spectra of the electrodes before and after cycling (1st, 5th, 10th, and 50th) are fitted by the equivalent circuit (Figure S11, Supporting Information), and the calculated R_{ct} and Warburg coefficient (σ) are listed in Table S2,S3, Supporting Information, respectively. The calculated σ and Na^+ diffusion coefficient show little difference between HC and CC-HC, indicating that the formation of closed pores does not significantly affect the process of sodium ion diffusion. Additionally, it can be seen that the R_{ct} of pristine HC and CC-HC are 299.3 and 249.8 Ω, respectively, whereas they sharply drop to 22.27 and 15.53 Ω after the initial cycle due to the formation process of the active material. In subsequent cycles, the change in R_{ct} is quite small, suggesting a stable electrode/electrolyte interface formed on the two electrodes. Note that the resistance of CC-HC is lower than that of HC throughout the cycling, which will benefit the fast charge–discharge kinetics.

As expected, the CC-HC electrode demonstrates much better rate capability than the HC electrode. Figure 4f displays the rate performance of the two electrodes at different current densities ranging from 0.1 to 10 C (1C = 250 mA g^{-1}). CC-HC delivers capacities of 253.9 and 239.2 mAh g^{-1} at 2 C and 8 C, evidently higher than those (176.0 and 146.8 mAh g^{-1}) of HC. In particular, the CC-HC electrode still provides a high capacity of 236 mAh g^{-1} even at 10 C, corresponding to 80% of its capacity at 0.1 C, implying its capability to sustain high current pulses under rapid discharge and charge conditions. Furthermore, when the current rate is back to 0.1 C, the capacity of CC-HC fully recovers due to its excellent structural stability and reversible sodium storage behavior. In addition to its exceptional rate capability, the CC-HC electrode also demonstrates excellent cycling stability. Figure 4g shows that CC-HC exhibits a high capacity retention of 98.4% after 300 cycles at a current density of 50 mA g^{-1}. Upon being

cycled at a higher current density of 200 mA g^{-1}, the CC-HC electrode can still retain 71.8% of the initial capacity after 800 cycles (Figure 4h). By comparison, the capacity retention of HC is 63.5%. It is worth noting that the average coulombic efficiencies of CC-HC and HC are 99.6% and 96.1%, respectively. The improved rate capability, electrochemical reversibility, and cycling stability are related to the closed-pore structure and decreased specific surface area of CC-HC, which further demonstrates the effectiveness of catalytic carbonization in constructing closed-pore structures of HC. Compared with HC anodes reported in previous works (Table S4, Supporting Information), CC-HC demonstrates its superiority in terms of ICE, reversible capacity, and cycling stability.

2.3. CC-HC||Na$_{0.67}$Ni$_{0.2}$Fe$_{0.2}$Mn$_{0.6}$O$_2$ Full Cell

As mentioned above, while synthesizing the CC-HC anode, theNa$_{0.67}$Ni$_{0.2}$Fe$_{0.2}$Mn$_{0.6}$O$_2$ (NNFM) cathode is also prepared from the mixed transition metal oxide catalysts. The electrochemical properties of the NNFM cathode are tested in the voltage range of 1.5–4.3 V. **Figure 5**a shows the CV curves of the NNFM cathode at a scan rate of 0.1 mV s^{-1}. It can be inferred that the broad redox peak in the potential region of 3.0–4.0 V corresponds to the fusion of the oxidation/reduction reactions of Ni^{2+}/Ni^{3+} and Fe^{3+}/Fe^{4+} redox couples, while the peaks below 2.5 V should be ascribed to the redox reaction of the Mn^{3+}/Mn^{4+} couple. The highly overlapped CV curves in the first three scans indicate that the NNFM cathode has a stable structure and electrochemical reversibility during cycling. The charge–discharge curves of NNFM at a current density of 52 mA g^{-1} are shown in Figure 5b. It can be seen that the NNFM cathode has an initial discharge capacity of 130 mAh g^{-1}, with almost no capacity decay in the first 10 cycles. Long-term cycling test in Figure S12, Supporting Information, shows the cathode has a capacity retention of 62.6% after 300 cycles, with an average coulombic efficiency of 98.7% at 130 mA g^{-1}. Figure S13, Supporting Information, provides the rate performance of NNFM at various current densities ranging from 26 to 520 mA g^{-1}, and the corresponding discharge capacities are 132.8, 123.3, 106.3, 94.2, and 75.7 mAh g^{-1}, respectively. Furthermore, SEM (Figure S14, Supporting Information) and XPS (Figure S15, Supporting Information) analyses are conducted to evaluate its structural stability. SEM images show that the cathode material particles maintain a smooth surface and no cracks after cycling. Additionally, the Mn 2p XPS spectra of NNFM show no significant shifts after cycling, indicating that the material can undergo reversible electrochemical reactions. Moreover, the comparison between NNFM and previously reported Fe, Mn-based transition metal oxide cathode materials in Table S5, Supporting Information, demonstrates that the sodium storage performance of NNFM is competitive, which enables it to couple with the CC-HC anode for the fabrication of a sodium-ion full cell.

Based on the simultaneously synthesized closed-pore-rich CC-HC anode and NNFM cathode, a CC-HC||NNFM full cell is then established (Figure 5c). Electrochemical tests of the full cell are performed within a voltage range of 1.5–4.2 V at a current density of 52 mA g^{-1}. It can be seen that the full cell delivers a
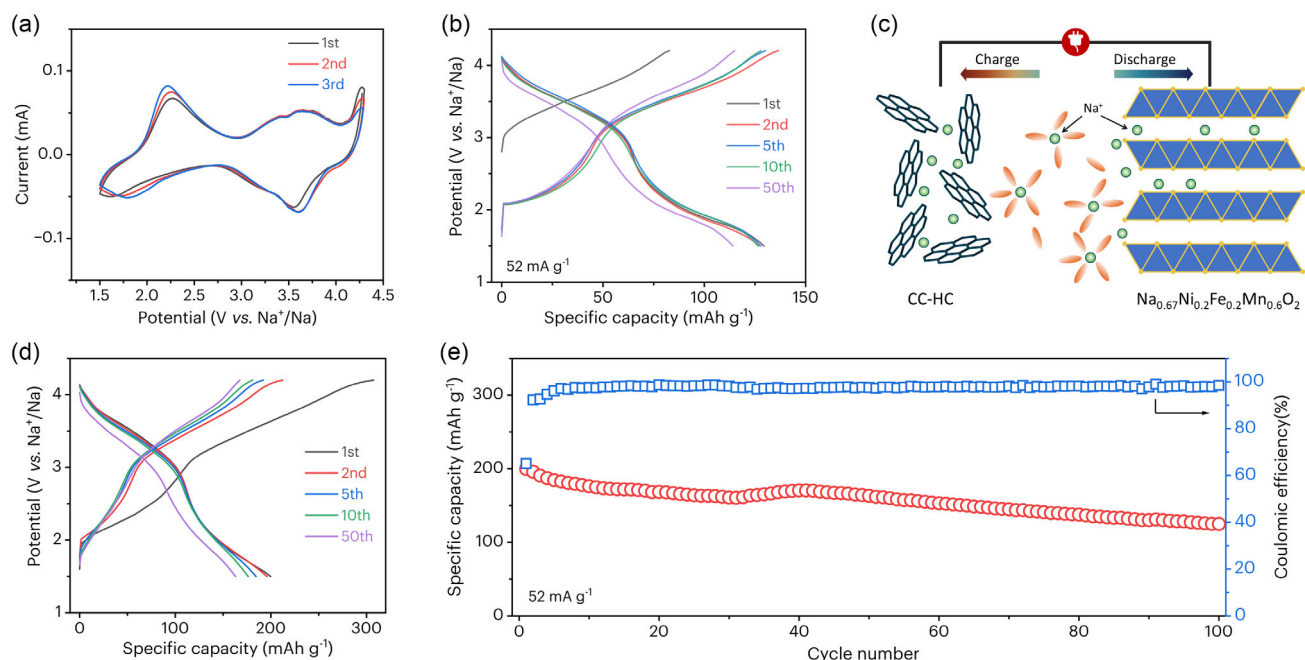
Batteries & Supercaps

Research Article
doi.org/10.1002/batt.202500715

**Chemistry
Europe**

European Chemical
Societies Publishing

Figure 5. a) The CV curves at 0.1 mV s^{-1}, and b) the discharge–charge curves at a current density of 52 mA g^{-1} of NNFM cathode. c) Illustration of CC-HC∥NNFM full cell. d) The discharge–charge curves, and e) cycling performance of CC-HC∥NNFM full cell at a current density of 52 mA g^{-1}.

reversible discharge capacity of 199.8 mAh g^{-1} (calculated based on the weight of CC-HC anode) with an average working voltage of 3.21 V (Figure 5d). When taking account of the overall weight of both cathode and anode materials, the energy density of the full cell reaches 206.7 Wh kg^{-1}. Figure 5e shows that a discharge capacity of 125 mAh g^{-1} is maintained after 100 cycles, corresponding to the capacity retention of 62.6%. The successful construction of sodium-ion full cells indicates that the strategy of simultaneously preparing high-performance anode and cathode materials proposed in this work has considerable practicability.

3. Conclusion

In this article, we propose a novel transition metal oxide catalytic strategy to prepare closed-pore-rich HC anode from walnut shell precursor while simultaneously transforming the metal oxide catalyst into layered oxide cathode. The abundant closed-pore structure in HC induced by the transition metal oxides catalytic effect provides an augmented array of sites for sodium-ion storage, thereby contributing to a heightened plateau capacity and coulombic efficiency. Consequently, the CC-HC anode exhibits a reversible capacity of 301.6 mAh g^{-1} with a high ICE of 92.34%. Besides, capacity retentions of 98.4% and 71.8% are achieved after 300 and 800 cycles, respectively. Note that a sodium-ion full cell is established based on the simultaneously synthesized CC-HC anode and NNFM cathode, which attains an energy density of 206.7 Wh kg^{-1} and superior cycling performance. This study not only develops a new strategy to regulate

closed-pore structure of HC by catalytic carbonization, but also provides a green and sustainable route for achieving high-performance SIB electrode materials.

4. Experimental Section

Material Preparation

The HC was synthesized by a two-step method. In the first step, a mixture of walnut shells and transition metal oxides (including NiO, Fe$_2$O$_3$, and Mn$_2$O$_3$, where the molar ratio was 2:1:3) was treated in an argon atmosphere at a temperature of 600 °C for 6 h. The resulting materials were then acid-washed to separate the metal oxides and carbon. In the second step, the carbon after drying was sintered at 1300 °C for 6 h in an argon atmosphere and the product was denoted as CC-HC. For comparison, HC is synthesized by the same method in the absence of transition metal oxides. The catalyst is acid-washed to form a metal salt solution, which is then mixed with NaNO$_3$, and the resulting solution is stirred and heated at 110 °C to obtain the powder. The powder is calcined at 950 °C in a dry air atmosphere for 10 h to obtain Na$_{0.67}$Ni$_{0.2}$Fe$_{0.2}$Mn$_{0.6}$O$_2$ (NNFM).

Material Characterizations

XRD (Rigaku MiniFlexll with a monochromated Cu Ka X-ray source) was applied to examine the crystal structures of anode and cathode materials. The structure morphologies were observed by a scanning electron microscope (SEM, Zeiss Merlin Compact) and a transmission electron microscope (TEM, JEM-2100). The element distribution of materials was obtained by energy-dispersive spectroscopy (EDS) paired with SEM mapping. XPS (ESCALAB250Xi, Thermo Fisher)

and Raman spectroscopy (DXR2, Thermo Fisher) were applied to investigate the element speciation and chemical bonding. The pore structure textures were characterized by adsorption–desorption measurements (Micromeritics ASAP 2460), and the SAXS (Xeuss 2.0) technique. The N_2 and CO_2 adsorption–desorption isotherms were respectively obtained at 77 and 273 K and analyzed by the density functional theory (DFT) method. The specific surface area was calculated based on the N2 adsorption isotherm by using the BET method. SAXS used a Pilatus 3R 300K detector equipped with a Cu kα radiation source of 30 W ($\lambda = 1.542$ Å), and the data were fitting to obtain the average pore size. The true density was measured by using the He replacement method.

Electrochemical Measurements

The HC anode electrodes were prepared by mixing 85 wt.% active material powder, 6 wt.% Super P, 4.5 wt.% sodium carboxymethyl cellulose (CMC), and 4.5 wt.% styrene butadiene rubber (SBR) to form a uniform slurry. Then, the slurry was coated on the Cu foil and dried at 80 °C for 10 h in a vacuum oven. While the NNFM cathode electrodes were prepared by mixing 80 wt.% active material powder, 10 wt.% Super P, and 10 wt.% polyvinylidene fluoride (PVDF) to form a uniform slurry, which was similarly coated onto Al foil and dried under the same conditions (80 °C, 10 h). The electrolyte used was 1 mol L^{-1} sodium hexafluorophosphate (NaPF$_6$) in diethylene glycol dimethyl ether (G2). Coin cells (CR2032) were assembled in an argon-filled glove box. Galvanostatic charge/discharge tests were conducted on a LAND CT-2001 test system. CV measurements were also carried out with the coin cell on an IviumNstat electrochemical workstation.

Computational Methods

Quantum chemical calculations were performed using ORCA (version 5.0.3). For each type of transition metal oxide cluster, 100 distinct initial configurations were generated using the genmer code. These configurations were then subjected to semiempirical energy calculations using the XTB. The lowest-energy structure identified from these calculations was selected as the input model for subsequent quantum chemical optimizations, which were carried out using the B3PW91 functional in combination with the def2-SVP basis set. The AIMD were performed using the Vienna Ab Initio Simulation Package (VASP). In the AIMD simulations, a plane wave basis set with a cut-off energy of 450 eV was utilized, and the time step was set to 1 fs. Gaussian smearing was applied with a smearing value of 0.1 eV. The convergence criterion for the self-consistent field energy was set at 1×10^{-4} eV. The interactions between electrons and cores were treated by using projector augmented wave (PAW) pseudopotentials, and the Perdew−Burke−Ernzerhof (PBE) method within the generalized gradient approximation (GGA) was adopted for the exchange-correlation potential. The sampling of the Brillouin zone was performed by using the Γ point.

Acknowledgements

Conflict of Interest

The authors declare no conflict of interest.

Data Availability Statement

The data that support the findings of this study are available in the *supplementary material* of this article.

[1] H. Wu, T. Wen, L. Chen, Y. Ding, X. Pu, Y. Cao, Z. Chen, *Small Methods* **2025**, *9*, 2400642.

[2] Z. Yang, J. Zhang, M. C. W. Kintner-Meyer, X. Lu, D. Choi, J. P. Lemmon, J. Liu, *Chem. Rev.* **2011**, *111*, 3577.

[3] P. Zibing, C. Huaqi, Z. Yubin, D. Yan, P. Xiangjun, C. Zhongxue, *Energy Mater.* **2023**, *3*, 300054.

[4] C. Liu, K. Chen, F. Li, A. Zhao, P. Liu, Z. Chen, Y. Fang, Y. Cao, *J. Am. Chem. Soc.* **2025**, *147*, 14635.

[5] X. Pu, S. Zhang, D. Zhao, Z.-L. Xu, Z. Chen, Y. Cao, *Electrochem. Energy Rev.* **2024**, *7*, 21.

[6] P. Barpanda, L. Lander, S.-i. Nishimura, A. Yamada, *Adv. Energy Mater.* **2018**, *8*, 1703055.

[7] C. M. Ghimbeu, A. Beda, B. Réty, H. E. Marouazi, A. Vizintin, B. Tratnik, L. Simonin, J. Michel, J. Abou-Rjeily, R. Dominko, *Adv. Energy Mater.* **2024**, *14*, 2303833.

[8] Y. Fang, Z. Chen, L. Xiao, X. Ai, Y. Cao, H. Yang, *Small* **2018**, *14*, 1703116.

[9] L. Chen, M. Chen, Q. Meng, J. Zhang, G. Feng, X. Ai, Y. Cao, Z. Chen, *Angew. Chem., Int. Ed.* **2024**, *63*, e202407717.

[10] M. Walter, M. V. Kovalenko, K. V. Kravchyk, *New J. Chem.* **2020**, *44*, 1677.

[11] Y. Chen, S. Yan, L. Chen, D. Zhao, Y. Ding, Y. Zeng, Z. Chen, *Small* **2025**, *21*, 2412681.

[12] S. Qiao, Q. Zhou, M. Ma, H. K. Liu, S. X. Dou, S. Chong, *ACS Nano* **2023**, *17*, 11220.

[13] Y. Sun, Q. Wu, X. Liang, H. Xiang, *Mater. Chem. Front.* **2021**, *5*, 4089.

[14] L. Xu, Y. Li, Y. Xiang, C. Li, H. Zhu, C. Li, G. Zou, H. Hou, X. Ji, *ACS Nano* **2025**, *19*, 14627.

[15] L. Xiao, H. Lu, Y. Fang, M. L. Sushko, Y. Cao, X. Ai, H. Yang, J. Liu, *Adv. Energy Mater.* **2018**, *8*, 1703238.

[16] X. Dou, I. Hasa, D. Saurel, C. Vaalma, L. Wu, D. Buchholz, D. Bresser, S. Komaba, S. Passerini, *Mater. Today* **2019**, *23*, 87.

[17] Z. Zheng, B. Pei, L. Zhang, X. Cao, S. Liang, *Energy Storage Mater.* **2025**, *75*, 104068.

[18] Y. Chen, H. Sun, X.-X. He, Q. Chen, J.-H. Zhao, Y. Wei, X. Wu, Z. Zhang, Y. Jiang, S.-L. Chou, *Small* **2024**, *20*, 2307132.

[19] L. Xie, C. Tang, Z. Bi, M. Song, Y. Fan, C. Yan, X. Li, F. Su, Q. Zhang, C. Chen, *Adv. Energy Mater.* **2021**, *11*, 2101650.

[20] Z. Tang, R. Zhang, H. Wang, S. Zhou, Z. Pan, Y. Huang, D. Sun, Y. Tang, X. Ji, K. Amine, M. Shao, *Nat. Commun.* **2023**, *14*, 6024.

[21] X. Chen, J. Tian, P. Li, Y. Fang, Y. Fang, X. Liang, J. Feng, J. Dong, X. Ai, H. Yang, Y. Cao, *Adv. Energy Mater.* **2022**, *12*, 2200886.

[22] Q. Meng, Y. Lu, F. Ding, Q. Zhang, L. Chen, Y.-S. Hu, *ACS Energy Lett.* **2019**, *4*, 2608.

[23] X. Li, H. Wang, X. Liu, Q. Liang, J. Hu, L. Xu, C. Ding, Y. Li, Y. Liu, Y. Gao, *J. Energy Storage* **2025**, *108*, 114995.

[24] Z. Wei, H.-X. Zhao, Y.-B. Niu, S.-Y. Zhang, Y.-B. Wu, H.-J. Yan, S. Xin, Y.-X. Yin, Y.-G. Guo, *Mater. Chem. Front.* **2021**, *5*, 3911.

[25] G. Liu, J. Yuan, H. Li, Z. Li, C. Hu, X. Qiao, M. Wang, B. Yuan, P. Zhang, Z. Wu, *ACS Appl. Mater. Interfaces* **2024**, *16*, 46226.

[26] X. Liu, K. Ding, K. Qian, H. He, Y. Wu, Y. Chen, Y. Wang, J. Zhang, B. Wang, *Chem. Eng. J.* **2025**, *510*, 161689.

[27] X. Li, N. Sun, S. Zhang, R. A. Soomro, B. Xu, *J. Mater. Chem. A* **2024**, *12*, 12015.

[28] W. Zhang, R.-R. Cheng, H.-H. Bi, Y.-H. Lu, L.-B. Ma, X.-J. He, *New Carbon Mater.* **2021**, *36*, 69.

[29] N. Sun, Z. Guan, Y. Liu, Y. Cao, Q. Zhu, H. Liu, Z. Wang, P. Zhang, B. Xu, *Adv. Energy Mater.* **2019**, *9*, 1901351.

[30] X. Zhao, Y. Ding, Q. Xu, X. Yu, Y. Liu, H. Shen, *Adv. Energy Mater.* **2019**, *9*, 1803648.

[31] A. C. Ferrari, J. Robertson, *Phys. Rev. B* **2000**, *61*, 14095.

[32] Y. Morikawa, S.-I. Nishimura, R.-I. Hashimoto, M. Ohnuma, A. Yamada, *Adv. Energy Mater.* **2020**, *10*, 1903176.

[33] S. Gan, Y. Huang, N. Hong, Y. Zhang, B. Xiong, Z. Zheng, Z. He, S. Gao, W. Deng, G. Zou, H. Hou, X. Ji, *Nano-Micro Lett.* **2025**, *17*, 325.

[34] X. Zhu, X. Jiang, X. Liu, L. Xiao, Y. Cao, *Green Energy Environ.* **2017**, *2*, 310.

[35] Q. Li, X. Liu, Y. Tao, J. Huang, J. Zhang, C. Yang, Y. Zhang, S. Zhang, Y. Jia, Q. Lin, Y. Xiang, J. Cheng, W. Lv, F. Kang, Y. Yang, Q.-H. Yang, *Natl. Sci. Rev.* **2022**, *9*, nwac084.